Egypt. J. Chem. **Vol. 68**, No. 3. pp. 63 - 78 (2025)

Egyptian Journal of Chemistry

http://ejchem.journals.ekb.eg/

Non-Isothermal Kinetics of Coats-Red Fern in the Critical Points: Formation of$Al_{2-x}Cr_xO_3$(x = 0.02) powders obtained by Sol-Gel Method

Fatah Hadji [1], Younes Rassim[1], D. Belfennache[2], R. Yekhlef[2],Nedjemeddine Bounar[3],Mohand Amokrane Bradai[1],Mohamed Hemdan[4],Mohamed A. Ali[4*]

[1]*University of Bejaia, Faculty of Technology, Laboratory of Mechanics, Materials and Energetic, 06000 Bejaia, Algeria.*

[2]*Research Center in Industrial Technologies CRTI, P.O. Box 64, Cheraga, 16014 Algiers, Algeria.*

[3]*Laboratory of the Interactions Materials–Environment, University of Jijel, 18000 Jijel, Algeria*

[4]*School of Biotechnology,Badr University in Cairo(BUC), Badr City 11829, Cairo, Egypt*

Abstract

In this study, ruby (Cr^{3+} doped Al_2O_3) was synthesized through the citrate method employing citric acid in excess as a chelating and fuel agent. The primary focus of our study was on two critical phase heat points, TPH, and TPD. The system was considered opaque, and we aimed to comprehend the behavior of crystal structure formation. Thermal kinetics was examined using the Coates-Redfern method, and various mechanisms were selected based on heating coefficients. Twenty-eight models were explored, combining the kinetics approach with experimental thermal analyses, including Thermogravimetry (TGA) and Differential Scanning Calorimetry (DSC).Kinematic parameters thanks to model fitting methods, were confirmed with a high R-squared coefficient of between (0.95 - 0.99). Despite slight differences and notable activation energy with reaction order, nucleation and subsequent random nucleation and diffusion mechanisms were revealed. Heat treatment showed consistency in Fourier transform infrared (FTIR) separation of the complex on aluminum and chromium oxides, indicating the presence of homo-bond decay upon treatment at 200-500-1000 °C. After the decomposition of the organic matter, the ceramic transforms into a green powder and subsequently transitions to a vividly crystalline pink color at a specific temperature of 1100 °C. All the surprising values found provide insight into the complexity of the crystallization process. It crystallizes in the hexagonal system in space group R-3c, according to analytical data from X-ray diffraction (XRD), however semi-investigation revealed that its morphological state is arbitrarily formed and ranges from 0.5 to 78 µm. Additionally, an elemental analysis study (EDS) verified the presence of Cr and O in the sample series.

Keywords: *Ruby*, Sol-gel, Citricacid, Coats-Redfern, Kinetics, Pink color.

1. Introduction

Ruby (Cr^{3+} doped Al_2O_3) is one of the many forms of α-Al_2O_3 that exists ceramics found in various applications in the industry [1 ,2]. Cr^{3+} substitutes for Al^{3+} in small amounts to maintain stability [3]. Commonly recognized as a solid solution. Such as high thermal, optical and mechanical resistance, etc. [4-6]. From recent applications, temperature sensors, lasers, masers, optoelectronics [7, 8]. It has been used as an effective coolant and as a reflective pigment for near-infrared radiation (NIR), in reversible thermal sensors and other related applications, used as a filter for luminous nanoparticles [9]. For this reason, researchers have turned their attention to environmentally friendly and low-cost manufacturing methods [10-12]. The goal was to discover new structures rather than cost-effectively produce them at slow melting and cooling points.Sol-gel is a wet chemical method for the synthesis of high-purity metal oxide nanoparticles, based on the dissolution of molecular precursors in water or an alcohol gel as a result of low-temperature hydrolysis/alkaline hydrolysis [13]. Citrate –nitrate is a non-alkoxide Sol-Gel. [14]. Because was used on the chelation reaction between bi-tern-quaternary oxides metal [15]. The formation of metal citrate complexes makes them stable, which takes shape in a three-dimensional structure. [16] Produces advantages of being easy, low cost, good homogeneity and high purity [15, 17].

*Corresponding author e-mail: mohamed.ahmed_ali@buc.edu.eg; (Mohamed A. Ali).

Received date 16 April 2024; revised date 10 July 2024; accepted date 28 July 2024

DOI: 10.21608/EJCHEM.2024.283147.9600

Citric acid is the fuel for the combustion stages of this uniform gel. [16, 18]. The decomposition and transformation of organic citrate residues occurs not only by combustion, but also by reaction with the nitrates present in the mixture [19-21].

On the other hand, the study of thermal kinetics is of paramount importance [22], as non-isotherms are often limited to a phase-specific temperature range, the crystallization behavior of the system being profoundly affected by the final structure[23, 24]. The aim is to achieve optimal, desirable performance and functional properties that meet the essence of our study, the realistic results of which depend on the preparation method.TGA its use in kinetic models is widely used whose accuracy of the parameters obtained depends on the degree of conformity to the chosen response model [25]. Most of the data in the literature on pyrolysis are sparse and limited and relate specifically to biomass as an alternative to conventional fuels [26].There are also different methods for studying data related to thermodynamic properties that are concerned with their decomposition kinetics [27] Herein, we report a selected the model fitting method, the Coats-Redfern approach with Cn (C: citrate method , n : type of model , n : 1….28) , Different reaction mechanisms were chosen to study using citric acid .

The Coats-Redfern method has been adopted to obtain optimum composition values with a single heating coefficient. It is explained in two critical points thermal occurs in the temperature range of TPH (25 to 187 °C) and TPD (187 to 550 °C) respectively, with the aim of evaluating the physical and chemical state of the chemical reaction order steps, acceleration rate, sigmoid rate equations, phase boundary reaction and diffusion mechanism, which contribute to ruby formation.

This study allows us to better elucidate what happens in the initial reaction sequence of dissociation of a citric complex with various cations (Al^{3+}, Cr^{3+}) during heat treatment, and enables the identification and characterization of reaction intermediates, which are often short-lived and difficult to detect by other means. The study of kinetics is fundamental to both theoretical and applied work. It provides insight into reaction mechanisms at critical points in nano forming transition reactions and, thanks to an understanding that enables the preparation of reaction conditions to be improved, more efficient, cost-effective, and safer chemical processes can be developed.In addition, this study gives us a future insight into how this gel can be used as a coating on stainless steel to enhance its surface structure and improve its physical and chemical properties.

2.Materials and experimental procedure

2.1. Preparation of Ruby Powder Cr-doped Al_2O_3

2.1.1. Preparation of Citrate Precursor Solution

The first precursors were aluminum nitrate ($Al(NO_3)3.9H_2O$) and hexahydrate chromium trichloride ($CrCl_3.6H_2O$), as indicated in table 1 ; these were dried in an oven at 110°C for two hours before being weighed. Stirring was continued until a clear, uniform solution was obtained that was violet in color. In accordance with the molar ratio (Al-Cr)/(citric acid) = 1/4 , citric acid is added to the mixture , in an acidic medium (pH=1,9) this is done with the help of nitric acid .

2.1.2. Formation of Citrate Gel

Over the course of five hours, the solution was continuously heated to 70 degrees Celsius under reflux conditions, removing excess water and allowing the gel to age before initiating the complexation reaction with citric acid to form stable complexes. The solution eventually turned into a gray colloidal solution with a purple dye.

2.1.3. Heat treatment

The resulting gel was dried in an oven at 100 and 200 degrees, ground into a powder, and placed inside a ceramic crucible. It was then calcined in a Nabertherm R50-300 outdoor tubular kiln, going through several stages and temperatures (300, 500, and 1000 degrees) for five hours. Afterwards, the sample was treated and calcined at 1000 degrees, yielding a green powder (Figure 1).

2.1.4. Crystallization

We chose the heat treatment zone for the sapphire crystallization step based on the results of thermal analysis (DSC-TGA) and the stability of sample interactions. The temperature was increased to 1100°C at a rate of 5°C per minute and maintained at this temperature for 15 h to achieve crystallization of the ruby phase.

Table .1: Detailed Specifications for Sol Gel – Citrate Precursors .

Precursor Name	Chemical Formula	Purity	Company	Physical State
Hydrated Aluminum Nitrate	$Al(NO_3)3•9H_2O$	99.99%	Sigma Aldrich	Solid
Hexahydrate Chromium Trichloride	$CrCl_3.6H_2O$	95%		Solid
Citric acid	$C_6H_8O_7$		Sigma Aldrich	Solid
Nitric Acid	HNO_3		Sigma Aldrich	Liquid

2.2 Characterization:

The thermo-kinetic properties of samples were analyzed through Thermo-gravimetric analysis (TGA) and differential thermal analysis (DSC). The study aimed to examine the thermal phenomena and decomposition steps of aerogels obtained after drying at 120°C. Thermo-gravimetric analysis-differential scanning calorimetry (TGA, DSC, SETARAM, SETSYS) was utilized, employing a linear heating rate equation from 25 to 1100°C in an air flow of 28 K/min. An FTIR study was conducted using a SHIMADZU8400S-FTIR instrument with KBr grain-based samples in the frequency range of 4000 to 400 cm^{-1}. Analyses were performed on samples treated at different temperatures (200, 500, and 1000°C), mixed with KBr. A blank disk (S = $1cm^2$) served as a reference, and all measurements were taken at room temperature under normal incidence. X-ray diffraction (XRD) characterization employed an advanced diffract meter, Mini flex 600, equipped with a cooler (lab tech/smart H150-1000), featuring a generator (600w, 40Kv, 15mA), Cu, Co, Cr tubes, and a scan speed of 0.01 to 100°/min (2θ). Crystal phase identification utilized the PANalytical ICSD database for High Score Plus and relevant phases from the PDF2 database. The morphology of the obtained ruby and corundum polymorphs was examined using a scanning electron microscope (SEM) with a tungsten filament, fully PC controlled, secondary vacuum pump, primary vacuum metalliser, and an industrial-grade nitrogen gas cylinder.

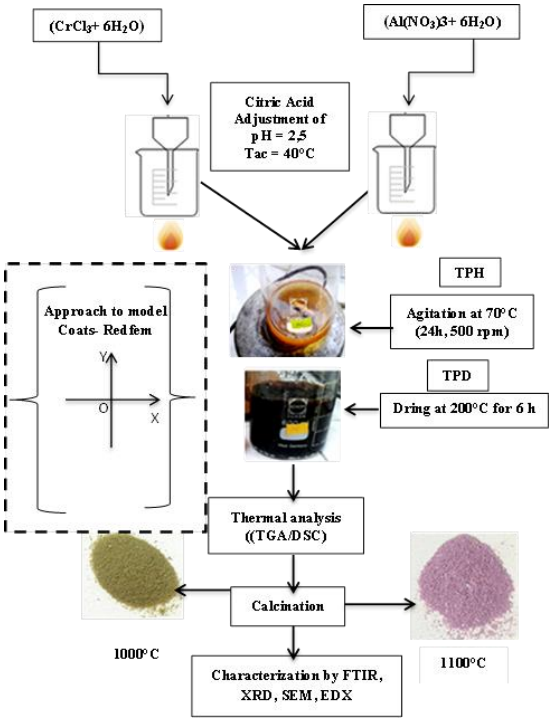

Fig.1: Schematic diagram summarizing the procedure for the kinetic study of the synthesis of rubies produced

2. Kinetics study

The thermal kinetics is related to the degree and type of reaction assumed for the dissociation analysis, and it is the most widely used method for the construction of the non-isothermal model [26]. The kinetics of the thermal decomposition of a sol gel and its staged crystallization, this was prepared by the complex citric acid. The decomposition rate of the non-isothermal solid is expressed mathematically.

3.1 Coats Redfern method

Mass kinetic studies of the gel complex were performed using the Coates-Redfern equation (Cotes et al, 1964), which was simulated activation energy and thermodynamic parameters were calculated Eq. (1) . [24,25].

$$ln\left(\frac{g(\alpha)}{T^2}\right) = ln\left(\frac{AR}{E_\alpha}\left(1-\frac{2RT}{E}\right)\right)\frac{E_\alpha}{RT} \qquad (1)$$

T : Absolute temperature (K) ,
α : Degree of conversion ,
R : Gas constant = 8.314 J/ (mol k^{-1}) ,
β : Heating rate (β = dT/dt) ,
E_a: Activation Energy (the least amount of energy required in a reaction to produce the end product), A : Pre-exponential factor (min^{-1})
In general, if $\frac{E_\alpha}{RT} \gg 1$ then $1-\frac{2\mathrm{RT}}{\mathrm{E}} = 1$ (approaching 1) hence Eq. (1) becomes

$$ln(\frac{g(\alpha)}{T^2}) = ln\left(\frac{AR}{E_\alpha}\right) - \frac{E_\alpha}{RT} \qquad (2)$$

Eqn. (2) shows a linear relation between $ln(\frac{g(\alpha)}{T^2})$ and $\frac{1}{T}$ for each g(α) shown in Table 1. Here we will plot the linear graphs $ln(\frac{g(\alpha)}{T^2})$ and $\frac{1}{T}$ by using the obtained data by TGA analysis for gel (Ci-Al-Cr) (Fig. 1) Decomposition at a heating rate of linear equation (R^2= 0.99) . Then by a linear graph of straight-line Eq. (1) upon comparing with the standard straight-line

$$y = c + bx,$$

We can find the slope $\frac{E_\alpha}{RT}$ and intercept

$$c = ln\left(\frac{AR}{E_\alpha}(1-\frac{2RT}{E})\right) (3)$$

All these calculations help to estimate the activation energy Ea and pre-exponential factors A by using R = 8.314 $Jmol^{-1}$ K^{-1}. We further calculate the thermodynamic parameters associated with mass decomposition.
Rate equations: Generally, the extent of the reaction can be calculated using the following relationship:

$$\alpha = \frac{m_0 - m_t}{m_0 - m_f} (4)$$

m_t : is the mass of the sample at any temperature t , **m_0** and **m_f**of the masses at initial and final temperatures respectively . Using the extent of reaction the rate of reaction can be calculated by using the relation in Eq. (4).
Table 2 shows the generally applied Reaction models (by putting a different value of n in Eqn. (1) for getting different reaction models in Coats-Redfern Method.

Tables 2- Various reaction mechanisms for study in Coats-Redfern Model. [26-29]

1-Order of reaction / Chemical Reaction

Models	f(α)	g(α)	Symbol of citrate rate
Zero-order	1	α	C1
One-third order	(3/2)(1 - α)1/3	1-(1 -α)2/3	C2
First-order	(1 -α)	-ln(1 -α)	C3
Three-quarters order	4(1-α)3/4	1-(1 -α)1/4	C4
Three-halves order	(1 -α)1/2	2[(1 -α)-1/2 -1]	C5
Second-order	(1 -α)2	(1 -α)-1 -1	C6
Third-order	(1 -α)3	0.5[(1 -α)-2 -1]	C7

2-Acceleratory rate equation / Nucleation

Mampel Power Law	(2 /3)α-1/2	α3/2	C8
Mampel Power Law	4 α3/4	α ¼	C9
Mampel Power Law	3 α2/3	α 1/3	C10
Mampel Power Law	2 α1/2	α ½	C11

3-Sigmoid rate equations or random nucleation and subsequent

Avrami-Erofeev equation n=1	(1-α)	-ln(1-α)	C12
Avrami model (n = 2/3)	1.5(1 -α) [-ln(1-α)]0.33	[-ln(1-α)]0.67	C13
Avrami model (n =1/2)	2(1 -α) [-ln(1-α)]0.5	[-ln(1-α)]0.5	C14
Avrami model (n =1/3)	3(1 -α) [-ln(1-α)]0.67	[-ln(1-α)]0.33	C15
Avrami model (n =1/4)	4(1 -α) [-ln(1-α)]0.75	[-ln(1-α)]0.25	C16

4-Deceleratory rate equations: Phase boundary reaction

Contracting Disk	(1 -α)0	α	C17
Cylindrical shape	2 (1 -α)0.5	1-(1 -α)0.5	C18
Sphere shape	3 (1 -α)0.67	1-(1 -α)1/3	C19

5-Based on the diffusion mechanism

1-D diffusion model	0.5α-1	α2	C20
2-D diffusion model	$[-\ln(1-\alpha)]^{-1}$	(1 -α) ln(1-α)+α	C21
3-D diffusion model	$1.5(1 -\alpha)0.33 [(1-\alpha)-0.33-1]^{-1}$	[(1-ln(1 -α))0.33]2	C22
3D-Ginstling–Brounshtein equation	$1.5[(1 -\alpha)-0.33 -1]^{-1}$	(1 -2α/3)- (1-α)2/3	C23
3D-Zhuravlev equation	3/2(1-α)4/3 [(1-α)-1/3-1]-1	[(1 -α) -1/3 -1]2	C24
3D-Jander equation	2(1– α)2/3 [1–(1 – α)1/3] –1	[1-(1 -α) 1/3]2	C25
3D-Anti-Jander	3/2[(1+ α)2/3[(1+α)1/3-1]-1	[(1+ α)1/3-1]2	C26
3D-Anti-Ginstling-	3/2[(1+ α)-1/3-1]-1	1+ 2/3α-(1+α)2/3	C27
3D-Anti-Zhuravlev, Lesokhin,	3/2(1+ α)4/[(1+α)-1/3-1]-1	[(1+ α)-1/3-1]2	C28

3.2 Thermodynamic parameters

The thermodynamic parameters of different stage to the ruby composite activation entropy (ΔS), activation enthalpy (ΔH) and Gibbs free energy (ΔG) were calculated in the pats of each thermal evolution using the following equations:

$$\Delta S = \ln(\frac{Ah}{KT})R \quad (5)$$

$$\Delta H = E_\alpha - RT \quad (6)$$

$$\Delta G = \Delta H - T\Delta S (7)$$

4. Results and discussion

4.1 Thermal Analysis

To understand the formation of formation noted ruby phase, the kinetic approach coupled to experimental thermal analysis TGA and differential scanning calorimetry (DSC),is a crucial parameter to study. The TGA curve (Fig. 2) of the aerogel mixtures (citric acid-Al-Cr) illustrates the phases of thermal decomposition and summarizes the kinetic phenomena occurring during the thermal treatment leading to the formation of ruby crystals.

This was proved by the DCS curve that shows the peaks of the type exo- or endothermic absorbing or emitting heat, and it was noted that the thermal phenomenon is divided into four sections: I, II, III and IV. In the first step I, the curves offer a slow decrease (9.38 %), in dissociation of the gel compound in the 70- 187 °C range of the sample, accompanied by a broad endothermic peak at about 118 °C. According to the literatures [29, 30] this change is primarily due to the removal of structural water, and it changes from a gel to a porous sponge resin. This stage is a key step in the reaction as it governs all thermo-kinetic phenomena. A significant weight loss of 78.1Observed at ~ 200°C, ~550°C, with a sharp endothermic peak at 330°C which corresponds to the combustion of citric acid organic matter to form CO_2 and H_2O, this result is in good agreement with those reported in [16].

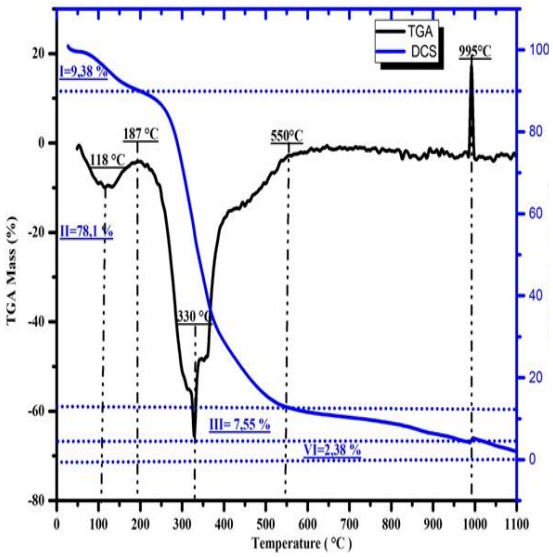

Fig. 2: Gravimetric thermal analysis (TGA) and differential analysis (DSC) of aerogel pyrolysis prepared by citrate method.

Based on works done by [16,31], in which nitrates are released in the order NO_2 followed by NO. The third stage is a small weight loss at the beginning of 600 °C, which is represented by the crystallization of aluminum oxide and the transition to a chromium γ-Al_2O_3 that turns green as shown by XRD at 1000 C°, leading to a slope level near zero.

At the DCS level with a sharp heat emission peak at 995 °C (endothermic), this gives the beginning of substitution of chromium atoms by aluminum more systematically to improve the crystallinity in the system.

The last stage, in which ruby is formed, as shown by X-ray analysis at 1100°C degrees, which take a pink color, see the form of 1 powder, and the loss of weight of chlorine residues is almost non-existent.

A plausible hypothesis that could explain this result is that the high temperature treatment in an aggressive medium lead to substitution of chromium atoms by aluminum more systematically to improve crystallinity in the ruby system.

4.2. Kinetics analysis

4.2.1 Fitting using the Coats-Redfern method

Typical curves have been drawn for the study points of the Coast-Redfern approach to determine the citric dissociation kinetic parameters that contribute to ruby synthesis at two critical points (TPH, TPD) and play an important role in determining the onset of crystallization and conferring physical and chemical properties.

The TGA profile of the gel decomposition into ceramic powders was analyzed using the kinetic parameters relevant to each approach, as summarized in the table showing 28 different models Figure 3 (a, b) shows the majority of the linear curves obtained by plotting 1/T versus ln [g(α)/T2] for different values of g(α).

These curves are predominantly linear, providinggreater precision for the analysis of thermal kinetic data. This approach, kinetic parameters, enables a deeper understanding of chemical reactions. The correlation coefficient between sets of values for each entity indicates the strength and direction of the linear relationship between the pairs. The closer the model ($R^2 = 1$), the better and more optimal the approach

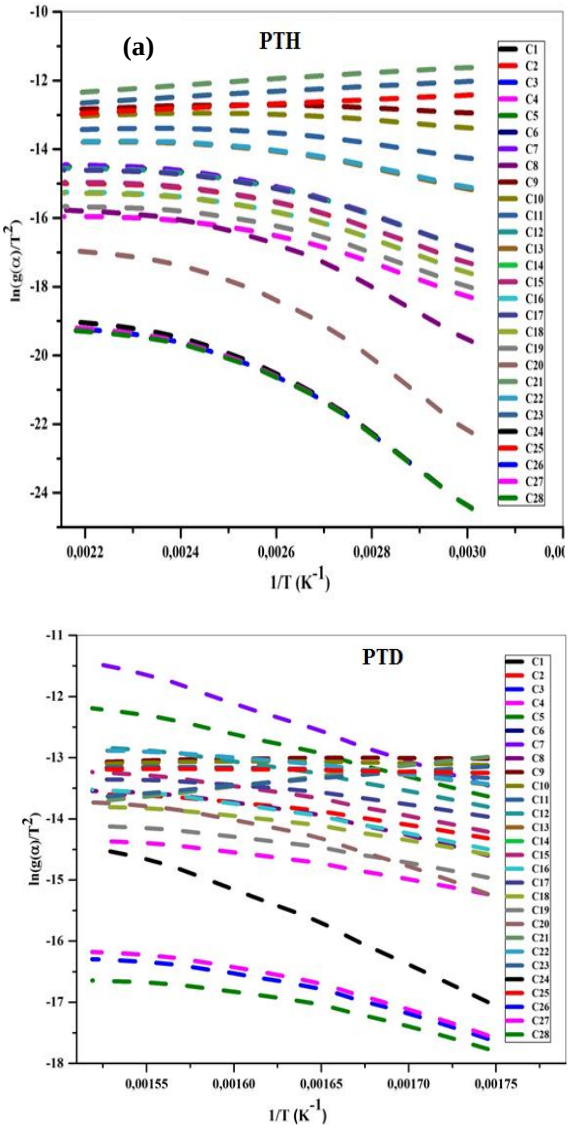

Fig. 3: The Coats Redfern $\ln(g(\alpha)/T^2)$, 1/T plots and fitting of non-isothermal crystallization of aerogel (a): PTD and (b) : TS01, at different 28 models .

These lines have distinct slopes, and the (R-square) values of their linear correlation coefficients range from 0,95 to 0,99 ,

-In GroupI, the reaction orders C1 and C4 exhibit dominant behavior during the TPH phase. Conversely, in the TPD phase, the reaction orders C2, C3, C5, C6, and C7 converge, showing closer proximity in their values. Notably, C7 demonstrates greater accuracy in representing the kinetic degradation of the mixture, making it a more reliable indicator.

-In Group II, the predominant nucleation pattern during the TPH stage is characterized by C8. However, at the TPD point, the C11 pattern emerges as the closest representation.

-In group GIII (GIII), the most common pattern in TPH is C15 and C16, followed by the predominance of C12, C13, and C14 in TPD.

-In Group IV (GIV), the phase boundary reaction is dominated by C17, C18, and C19 at both the TPH and TPD phases .

-In Group V (GV), based on the diffusion mechanism, C20, C21, C22, and C24 predominate during the TPD phase, while C23, C25, C26, C27, and C28 dominate during the TPH phase.

These values indicate the ideality of these models. In contrast, there are two inconsistent C9-C10 models , with R2 values below 0,5

These results indicate the fit of the models. The closer the R2 values are to 1, the stronger the correlation, signifying a better alignment between the experimental data and the proposed model. This analysis allows for the identification of the most reliable

models to describe the phenomenology of gel dissociation, while highlighting any differences or inconsistencies within the studied groups.

among the groups (G-I to G-V): Minimal variance was observed between the different groups. However, G-III shows a slight decrease in R2 values compared to the other group.

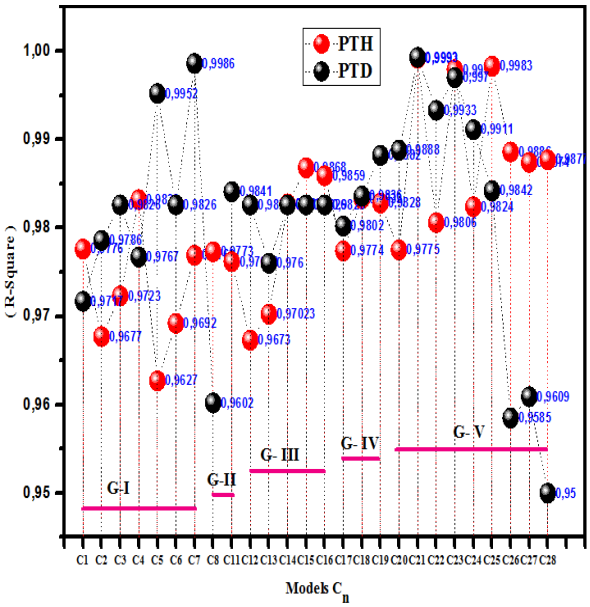

Fig. 4. Results of the R-squared (R^2) curve of independent variables values of fit in regression models.

Figure 4 shows that the model used to analyze the data is consistent with most points in the PTH and PTD groups. The slight variation in some values could be due to factors such as sample variability, experimental conditions, or measurement accuracy. The graph demonstrates the excellent performance of the models, with most R2 values approaching in one .

The graph fig.5illustrates variations in activation energy with positive values across the different models. These variations may reflect differences in how each model characterizes the dissociation process or disparities in the activation energy efficiency for the studied data points.When comparing the groups (PTH , PTD), the observed differences in activation energy values, ranging from 6 to 73 kJ/mol, may provide insight into how the two groups respond under distinct experimental conditions. Lower activation energy values typically indicate a more stable process.

Figure 6 shows that most of the free energy values are positive, which explains that both reactions are endothermic. The free energy values at the first critical point in the PTH phase are higher than the free energy values in most models in the PTD phase, indicating that the dissociation of water and the formation of 3D aerogel requires more energy to be released. In contrast, in the second stage, citric acid and nitrate are used as self-fuel and contribute to the crystallization of polycrystalline alumina reducing the free energy. According to the literature [19]

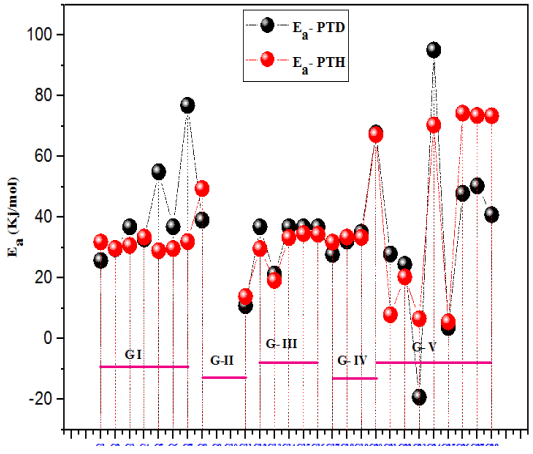

Fig. 5: Comparative of the Gibbs Energy Variation as a function of Coats-Redfern Models of Graphical Analysis

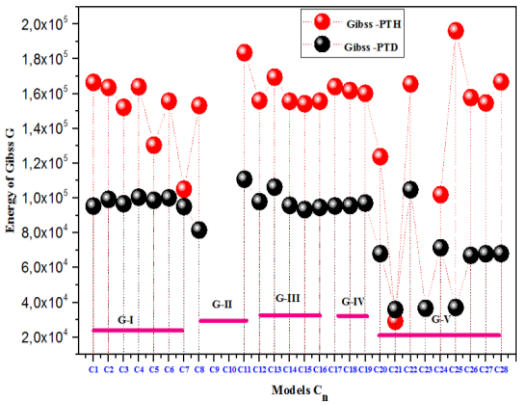

Fig. 6 : Graphical Analysis of the Gibbs Energy Variation as a Function of Coats-Redfern Models

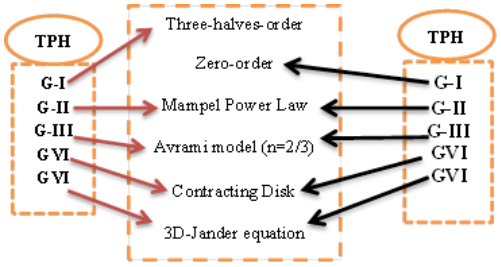

Fig.7. Positioning of critical points **(TPH ,TPD)** in the process of Ruby formation according to the stable activation energy

Table .3: representing the different linear fitting parameters of each thermal transition (TPH) of the samples with the 28 models of Coats-Red fern method .

Models	Slope	Intersect	A (1/min)	Ea (Kj/mole)
C1	-3830,01	-5,26	0,55642	31,84278
C2	-3569,96	-6,39	0,16754	29,68069
C3	-3690,98	-5,64	0,36677	30,68688
C4	-4025,61	-6,93	0,11359	33,46892
C5	-3485,50	-6,20	0,19765	28,97849
C6	-3565,43	-6,66	0,12719	29,64306
C7	-3844,75	-5,19	0,599	31,96529
C8	-5944,52	-1,45	38,85257	49,42274
C11	-1670,82	-9,19	0,00477	13,89124
C12	-3569,83	-5,97	0,253	29,6796
C13	-2302,78	-8,13	0,01886	19,14533
C14	-4007,88	-5,44	0,4847	33,32152
C15	-4160,09	-4,72	1,03174	34,58702
C16	-4127,81	-5,10	0,70065	34,31867
C17	-3823,94	-5,27	0,54612	31,79224
C18	-4024,87	-5,40	0,50849	33,46282
C19	-4008,59	-5,85	0,32292	33,32742
C20	-8080,24	2,41	2523,30861	67,17913
C21	-948,64	14,41	$4{,}83602*10^{7}$	7,88707
C22	-2441,72	-7,70	0,03088	20,30053
C23	-789,83	14,37	$3{,}86737*10^{7}$	6,56668
C24	-8466,72	1,32	890,20216	70,39237
C25	-663,67	14,40	$3{,}35934*10^{7}$	5,51779
C26	-8933,74	2,60	3393,57906	74,27517
C27	-8837,94	2,33	2567,42637	73,4787
C28	-8829,20	2,30	2468,01489	73,40601

Table .4 : representing the different linear fitting parameters of each thermal transition (TPD) of the samples with the 28 models of Coats-Red fern method .

	Slope	Intersect	A (min^{-1})	Ea (Kj/mole)
C1	-3096,11	-8,50	0,017	25,74106
C2	-3557,36	-8,06	0,031	29,57597
C3	-4428,76	-6,00	0,305	36,82079
C4	-3954,89	-8,24	0,028	32,88101
C5	-6609,73	-2,06	23,56	54,95333
C6	-4428,76	-6,69	0,15	36,82079
C7	-9236,63	2,65	3685,57	76,79342
C8	-4698,28	-6,26	0,249	39,06151
C11	-1302,61	-11,04	0.0005	10,82993
C12	-4428,76	-6,76	0,14246	36,82079
C13	-2561,97	-8,92	0,00958	21,30023
C14	-4428,76	-6,69	0,15296	36,82079
C15	-4428,76	-6,41	0,20393	36,82079
C16	-4428,76	-6,69	0,15296	36,82079
C17	-3334,95	-8,09	0,02837	27,72682
C18	-3860,79	-7,78	0,04495	32,09861
C19	-4214,32	-7,55	0,06182	35,03788
C20	-8142,11	-0,94	88,69947	67,69351
C21	-3351,71	18,82	$1,4116*10^{10}$	27,86603
C22	-2944,14	-8,273	0,02104	24,47762
C23	2316,44	-17,16	$-2,2722*10^{-6}$	-19,25889
C24	-11434,67	3,08	6980,35208	95,06786
C25	-442,28	-12,47	$4,72053*10-^{5}$	3,67713
C26	-5755,56	-7,38	0,10017	47,85177
C27	-6049,00	-6,81	0,18613	50,29143
C28	-4911,60	-9,02	0,01651	40,8351

Figure 6 shows that most free energy values are positive, which explains why both reactions are endothermic and not spontaneous. The free energy values in the first PTH critical point are higher than those of the free energy in most models at this PTD stage, indicating that water dissociation and the formation of three-dimensional aerogels require more released energy. In contrast in the second stage, citric acid and nitrates are used as auto fuel and contribute and crystallization, polycrystalline alumina which reduces the free energy. According to the literature [19] the most thermal reactions and physical and chemical properties that show a positive value for ΔG.

The reaction involved in decomposition at critical points is not spontaneous and requires heat. In most models, the activation energy tends to be low, and the Gibbs energy is high. This provides detailed and crucial research information, and the Cr-doped Al_2O_3 property can be applied to the thermochromic effect in sensing devices across the temperature range. These sensors can be used not only to warn users of potential damage due to high temperatures but also to monitor temperatures in various devices, such as aircraft engine components, heating panels, and furnaces. In addition, the presence of additional interactions involving Cr^{3+} ions may contribute to the partial quenching of luminescence [34]

4.3 Infrared Analyzes (FTIR)

Figure (8) shows the analytical FTIR spectra that was produced after treating the gel at the temperatures (a-200, b-500, and c-1000 °C), illustrated in the following curves. In the second parts of decomposition gel, it can be seen from the method of its preparation that there is water, organic substances, various chemicals, bonds, impurities and metal oxides, as shown in figure 3.

The absorption peaks common to all three samples at 3500-3300 and 1635 cm^{-1} that appear in all spectra are necessary due to the non-chemical stretching of the -OH group bond and bending vibrations [31].

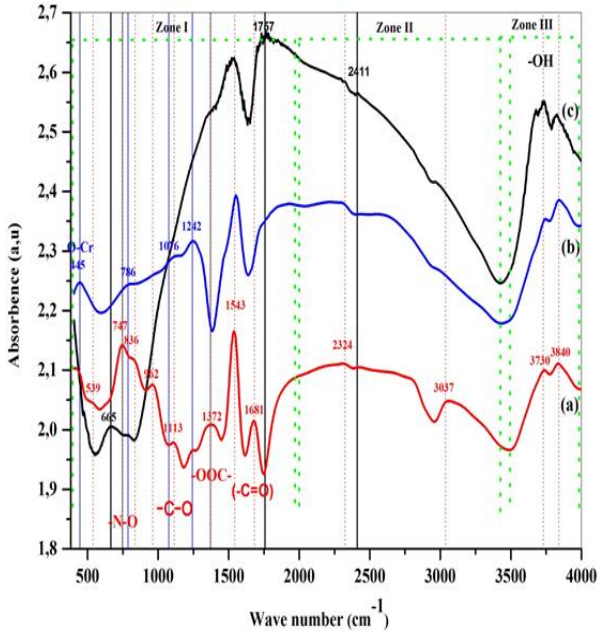

Fig .8: FTIR spectra of aerogel samples treated at different temperature, between the range 4000 and 400 cm^{-1}, (a) : 200°C ,(b) : 500°C , (c) : 1000°C.

The expansion modes of the carboxylate in the range 1384-1433 and 1597-1603 cm^{-1}, respectively, indicate the symmetrical and asymmetrical expansion of the C = O band in the metal carboxylate as shown in the table (See Table 3), confirming the chelation of Al^{3+}, Cr^{3+} and citric acid . When we raise the temperature to 500 °C, organic matter and nitrate decompose in the form of CO_2, H_2O, NO_2 and some absorption bands atrophy, as shown (b). The peaks at 829, 589 and 449 cm^{-1} are attributed to the vibrations of AlO_6, indicating the formation of α-Al_2O_3. On the other hand, the peaks at 762 cm^{-1} are attributed to the bending vibration of Al-O-Al , are attributed to the stretching and bending vibrations of Al-O, respectively, indicating the formation of θ-Al_2O_3 .The band at 480 cm^{-1} is attributed to the angular deformation of O- Al (OH), and the angular bending (OH)-Al-O gives rise to the peak at 633 cm^{-1}, and 746 cm^{-1} which is attributed to the stretching vibrations of AlO Al in the deformed AlO_6.

Table 5 - FTIR data of different bands

	Bands (cm^{-1})	Vibration mode	**Refs**
Citric acid	1210-1320 / 118-1210	-C-O (sy) in carboxylic acids	**[34,35]**
	1390-1550	-C= O(sy)	
	1681-1760	-C=O (sy ,b-asy b) (sy) in carboxylic acids H-bonded	
	430, 460, 570, 643 and 685	Attributed to Cr-O.	**[36]**
Nitrate	1530–1480 , 1290–1250 , 1035 –970 1565–1500 , 1300–1260 1040–1010 .	M-O-NO_2 mono-dentate nitrate M-O2-NO bi-dentate chelating nitrate.	**[37]**

4.3 X-ray diffraction analysis

Figure9 shows the XRD patterns of the green powder (0.02 Cr:Al_2O_3) peaks obtained for the composite at the annealing temperature of 1000 °C . The latter confirmed the existence of peaks that recognize the sequence (2θ : 19,951 , 33,675 , 36,684 , 44,796 , 67,308) , each one indicates different phases crystalline in a row , Aluminium Oxide – Theta (ISCD : 98-008-2504) , Eskolaite (ISCD : 98-003-3642) , Chromium(II) Dichloride (ISCD : 98-024-6418) , Aluminium Oxide (2.4/3.6) – Theta (ISCD : 98-006-6560) . The multiplicity of these compounds and the presence of chlorine showed that Cr+3 did not enter the alumina matrix and therefore crystallized poorly.This phenomenon can be attributed to the thermo-thermal diffusion peak at 955°C, likely associated with the dissociation of chlorine impurity residues. Chlorine typically influences the synthesis parameters, which in turn affect the crystallization process—a critical step in determining the crystallization parameters. Furthermore, the presence of chlorine bound to chromium dioxide hinders the incorporation of chromium into the alumina network. The larger ionic radii of Cr^{3+} and Al^{3+} compared to other ions may also contribute to a reduction in the structural order of the alumina [34].

X-ray diffraction Fig.10shows crystallinity at 1100°C and good agreement with the reference XRD pattern with the compound name Aluminum Oxide – Theta , ISCD : (98-008-2504) , while another crystal structure begins to appear a major phase noted Corundum ($Al_{1.98}$ $C_{0.02}O_3$) according to the ISCD : (98-002-0856) in the parameter crystalline of hexagonal and space group R-3C. The crystal structure improves compared to the previous sample, which changes the color of the ceramic from green to pink, Duy Khiem Nguyen and all Refers to this type of aluminum oxide tinged with a small amount of chromium is known as "ruby" or "ruby solution" and can be used as a thermochromic material[30].

The formation of a chromium-doped alumina solid solution is more difficult. According to, *Martos et al* [26] reported the formation of pink $Al_{2-x}Cr_xO_3$ solid solutions from Al_2O_3 and Cr_2O_3 after annealing at 1200 ° C. According to Shannon, the ionic radius of six Al^{3+} (0.535 Å) coordinated to the fold is smaller than that of Cr^{3+} (0.615 Å). Therefore, replacing Al^{3+} with larger Cr^{3+} ions increases the unit cell parameters and unit cell volume.

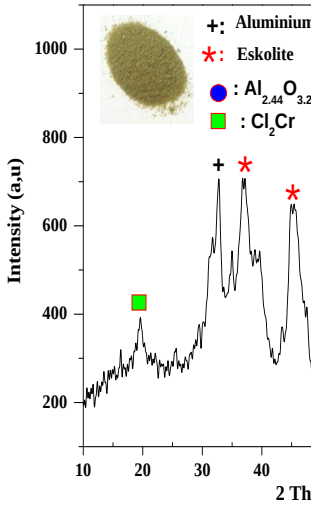

Fig.9: XRD patterns of annealed Green sample treated at 1000°C .

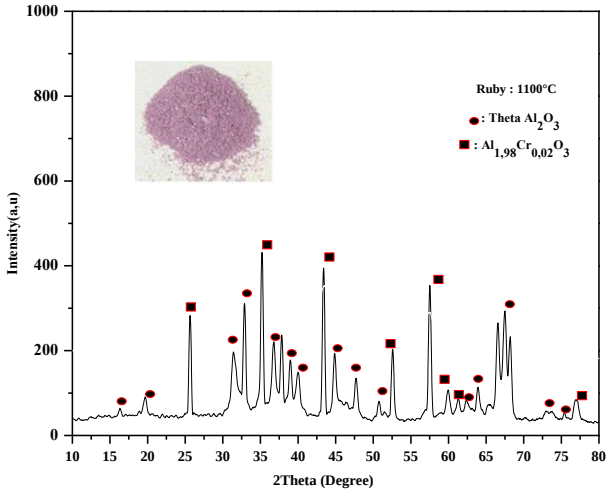

Fig.10: XRD patterns of annealed ruby $Al_{1.98}$ $Cr_{0.02}$ O_3sample treated at 1100°C .

4.5. SEM analysis:

The two images (Fig .11), provided show the sample under a scanning electron microscope (SEM) treated at a different temperature according to this difference. The powders have a layered, scaly structure with what appear to be sheet-like formations. These layers are irregular and appear to overlap, suggesting a complex, non-uniform surface. The layers are irregular and seem to overlap, suggesting a complex, uneven surface. Surface texture: The surface texture is rough with visible ridges and valleys. This type of texture can affect the material's properties. The photo shows areas where there are gaps or voids between laminates or layers. These voids show the presence of gaps of various sizes. Chlorine can prevent citric acid

from forming homogeneous complexes with aluminum, and chromium of different sizes can affect the morphology of poor crystallization. The activation energies also give a sense of the stability of the reaction, which was influenced by crystalinity and 3D diffusion (Fig.12).

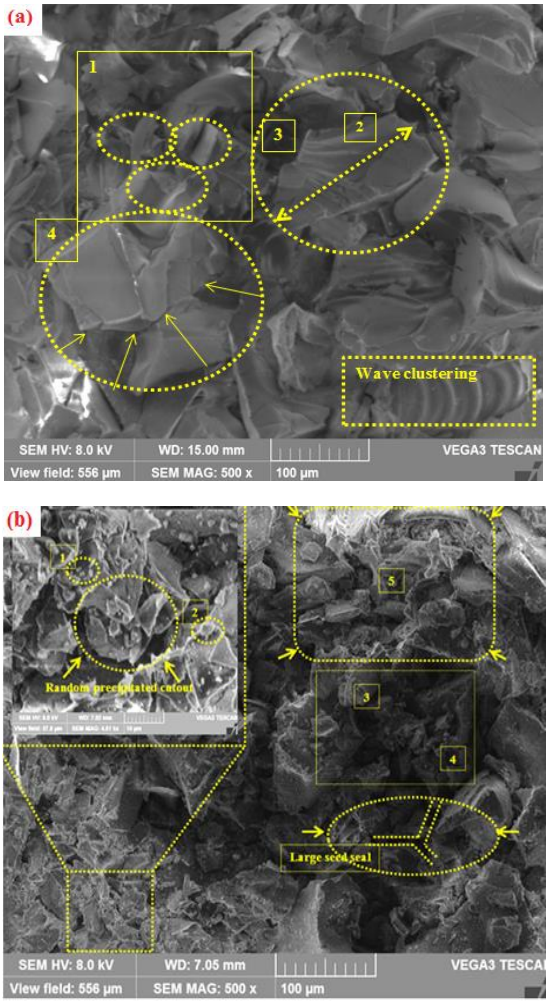

Fig. 11SEM images :
(a) : Green powder treated at 1000 ℃ ; (1) : Crystals with ill-defined and unorganized faces. (2): Irregular crystal with a rough, unstable surface size 90-146 µm. (3) :Interstitial spaces ; (4): Layered formation of varying microscopic structures .
(b) : SEM image of Ruby powder treated at 1100 ℃ ; (1) : Semi-spherical grain groups (size 0.5-1.1 µm) . (2) : Seed on interconnection isolated (size 2.5 µm) ; (3) , (4) : Mixed form Free (size 21- 36 µm) ; (5) : Compacted mixed form (size 38-59 µm).

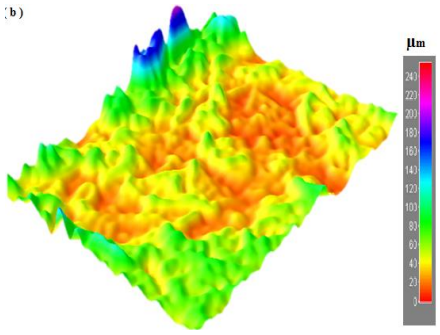

Fig.12: 3D modeling of morphology , distribution and microstructure the ruby powder.

4.6 EDAX analysis :

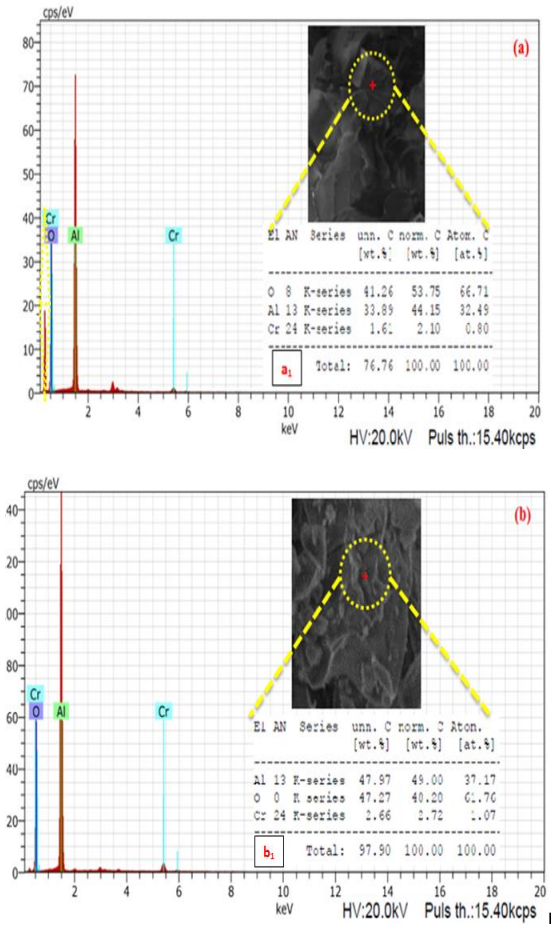

Fig.13: EDX result of $Al_{1,98}$ Cr $_{0,02}$ O_3 sample annealed treated at differents temperature : (a) at 1000 °C ,(b) at 1100°C for 15 hors.

Fig. 13:(a-b) indicates that oxygen is the main component of the sample. Aluminum is the main metallic element in the sample.(Cr^{3+}) indicates the presence of a small amount of chromium (show table a_1, b_1) .

Based on mass and atomic ratios, the sample consists mainly of oxygen and aluminum, with a trace of chromium. This proportional composition confirms the formation of aluminum oxide (Al_2O_3) with chromium impurities.The information is presented in the figures. According to these spectra, there is a spectrum when treated at 1000°C which suggests the presence of impurities such as carbonaceous chlorine peroxide. This prevented chromium particles from entering the aluminum matrix, which was revealed by thermal analysis in the presence of the peak at 995. In addition, X-ray analysis revealed amorphous crystallization with low crystallinity. Increasing the treatment temperature to 1100°C gives a positive perspective on the process of diffusion and replacement of the Cr^{3+} chromium atom by Al^{3+}aluminium, resulting in hybridization and improved crystal structure. It also confirms the formation of aluminum rubies at low temperatures compared with some of the mentioned research [38].

The high temperature allows chromium to diffuse into the alumina and homogenize its proportions, leading to the formation of new compounds or transformations in the crystalline structure Al $_{1.98}$ Cr $_{0.02}$ O_3.

4. Conclusions

Citric acid is chosen because it is readily available, inexpensive and has significant complexing properties. This type of chemical improves thermal stability and acts as a thermal fuel during the combustion phase in the presence of nitrates, which was confirmed by comparing the FTIR spectrum of the three samples at different temperatures, showing its disintegration at 500 °C. The pyrolysis of the block is studied by thermogravimetry at a heating rate of 28 ◦C/min. Thermal, kinetic and

thermodynamic parameters. It is calculated by a model fit of the Coats-Redfern method using 28 equations with two critical points, which can give an approximate result on the possibilities of evaluating thermodynamic parameters and increase the uncertainty of what happens inside any Ruby kinetics and improve calorific values. This technique allows us to estimate the activation energy potential for each approach and the closest approach to improving the thermal stability of the crystallization phase. The study could help further explore how heat and mass treatment can control the thickness of ruby ceramic coating deposits on substrates. We also hope that these results will contribute to monitoring the processes involved in the preparation of ceramics and composite materials based on $Al_2O_3:Cr^{3+}$.

5. References

[1] K. Boonin, W. Songpakob, N.S. Aminah, J. Kaewkhao, Fabrication of ruby by flame fusion technique and their properties.*Mater. Today: Proc*. 5(7), 15010-15013 (2018); https://doi.org/10.1016/j.matpr.2018.04.047

[2] S. Kumari, A. Khare,Optical and structural characterization of pulsed laser deposited ruby thin films for temperature sensing application.*Appl. Surf. Sci*.265, 180-186 (2013) https://doi.org/10.1016/j.apsusc.2012.10.163

[3] V. P. Dotsenko, I. V. Berezovskaya, N. I. Poletaev, M. E. Khlebnikova, I. V. Zatovsky, K. L. Bychkov, O. V. Khomenko, N. P. Efryushina,Combustion synthesis and nontrivial luminescence properties of nanosized δ*-Al_2O_3dopedwith Cr^{3+}ions*Prog. Photovolt.: Solid State Sci*. 119, 106704 (12). (2021);https://doi.org/10.1016/j.solidstatesciences.2021.106704

[4] N. Mironova – Ulmane, M.G. Brik, J. Grube, G. Krieke, M.Kemere, A. Antuzevics, E. Gabrusenoks, V. Skvortsova, E. Elsts,A. Sarakovskis, M. Piasecki, A.I. Popov,EPR, optical and thermometricstudies of Cr^{3+} ions in the α-Al_2O_3synthetic single crystal*Optical Materials*, 132. 112859 (2022); https://doi.org/10.1016/j.optmat.2022.112859

[5] K. Drdlikova, R. Klement, D. Drdlik, D. Galusek, K. Maca,Processing and properties of luminescent Cr^{3+} doped transparent alumina ceramics*J. Eur. Ceram. Soc*.40, 2573–2580 (2020).https://doi.org/10.1016/j.jeurceramsoc.2019.11.010

[6] Myrtille O.J.Y. Hunault, Y. Harada,J. Miyawaki,J. Wang, A. Meijerink, F. M. F. de Groot, M. M. van Schooneveld, Direct Observation of Cr^{3+} 3d States in Ruby: Toward Experimental Mechanistic Evidence of Metal Chemistry.*J. Phys. Chem. A*. 122, 4399−4413 (2018) DOI: 10.1021/acs.jpca.8b00984

[7] P. M. Lewis, Keerthana N, Deepak Habbar N, K.S. Choudhari, Sureh D. Kulkarni, Cr^{3+} doped Al_2O_3 nanoparticles: Effect of Cr^{3+} content in intensifying red emission. *Curr.Appl. Phys*.,32, 71-77(2021). https://doi.org/10.1016/j.cap.2021.10.003

[8] B. Ratzker, A. Wagner, B. Favelukis, S. Goldring, S. Kalabukhov,N. Frage,Optical properties of transparent polycrystalline ruby (Cr:Al_2O_3) fabricated by high-pressure spark plasma sintering. *J. Eur. Ceram. Soc.* 41(6).3520-3526 (2021). https://doi.org/10.1016/j.jeurceramsoc.2021.01.022

[9] G. Rani, P.D. Sahare, Structural and photoluminescent properties of Al_2O_3: Cr^{3+} nanoparticles via solution combustion synthesis method. *Adv Powder Technol*. 25(2), 767-772 (2014) https://doi.org/10.1016/j.apt.2013.11.009

[10] S. Zaiou, O. Beldjebli, D. Belfennache, M.Tayeb, F. Zenikheri, A. Harabi,Effect of CaF_2 addition on the densification behavior and mechanical properties of resistant anorthite and its bioactivity, *Dig.J.Nanomater. Bios*.18(1). 69-82 (2023). DOI: 10.15251/DJNB.2023.181.69

[11] O. A. Capeloto , N. E. de Souza, I. A. Santos, N. G. C. Astrath, I. T. P. Miranda, L. A. Pilatti, A. A. W. Hechenleitner, E. A. G. Pineda, M. A. C. de Melo, Preparation, structural and spectroscopic study of sol‑gel‑synthesized Cr^{3+}:Al_2 O_3 powder. SN Applied Sciences. 1, 1597 (2019) https://doi.org/10.1007/s42452-019-1631-9

[12] M. O. Paskhin, K. O. Aiyyzhy,R. V. Pobedonostsev, D. V. Kazantseva I. I. Rakov, E. V. Barmina, E. V. Yanykin, S. V. Gudkov, Ruby Nanoparticles for Greenhouse Farming: Synthesis, Features and Application. J. Compos. Sci. 8(1), 7 (2024). https://doi.org/10.3390/jcs8010007

[13] A. Sharma, P. Yadav, B. Khan, P. Kumar, M. K. Singh, Structural, electrical and optical properties of $Ca_{0.5}Sr_{0.5}SnO_3$ nanoparticle prepared by sol-gel method*Mater. Today: Proc*. 82, 308 313(2023).https://doi.org/10.1016/j.matpr.2023.02.007

[14] M. B. Polla , J. L. Nicolini , J. Venturini, A. C. Viegas , M. A. Z. Vasconcellos , O. R. K. Montedo , S. Arcaro.Low-temperature sol–gel synthesis of magnetite superparamagnetic nanoparticles: Influence of heat treatment and citrate–nitrate equivalence ratio.*Ceramics International* 49 7322–7332 (2023).https://doi.org/10.1016/j.ceramint.2022.10.182

[15] A. E. Danks , S. R. Hall, Z. Schnepp, The evolution of 'sol–gel' chemistry as a technique for materials synthesis.*Mater. Horiz*, 3, 91-112 (2016). DOI: 10.1039/C5MH00260E

[16] A. Babu , D. Tirumalarao , S. Das , V. Dixit , S.P. Sruthy , V. Vijayan, D. Jaiswal-Nagar,Effect of pH variation on citrate nitrate sol-gels obtained from auto-combustion method: Synthesis, calculations and characterisations of extremely dense $BaZrO_3$ceramic.*Open Ceramics*, 12, 100303 (2022).https://doi.org/10.1016/j.oceram.2022.100303

[17] Y. Wang , H. Li , D. Huang , X. Wang , L. Cai , Y. Chen , W. Wang , Y. Song , G. Han , B. Zhen,A high-performance ethanol gas sensor based on Ce-doped SnO_2 nanomaterials prepared by the Pechini method.*Mater. Sci. Semicond. Process*. 137, 106188 (2022).https://doi.org/10.1016/j.mssp.2021.106188

[18] V. Hiranmayee , K. Ananthasivan, D. Maji , K.Joseph,Microwave-assisted citrate gel-combustion synthesis of nanocrystalline urania.*J. Nucl. Mater*. 516, 73-83 (2019).https://doi.org/10.1016/j.jnucmat.2018.12.031

[19] D.K. Nguyena, Quang-Vu Bach, B.Kim, H. Lee, C. Kang, In-Tae Kim,Synthesis of Cr-doped Al_2O_3 by Pechini sol-gel method and its application for reversible thermochromic sensors*Mater. Chem. Phys*. 223, 708–714 (2019).https://doi.org/10.1016/j.matchemphys.2018.11.070

[20] R. Ianoș, E. Muntean, R. Băbuță, R. Lazău, C. Păcurariu, C. Bandas, *Ceramics International* 43(2), 2568–2572 (2017).https://doi.org/10.1016/j.ceramint.2016.11.061

[21] M.G. Tsegay , H.G. Gebretinsae , Z.Y. Nuru, Structural and optical properties of green synthesized Cr_2O_3nanoparticles.*Mater. Today: Proc.* 36, 587–590 (2021).https://doi.org/10.1016/j.matpr.2020.05.503
[22] D. Belfennache, D. Madi, R. Yekhlef, L. Toukal, N. Maouche, M.S. Akhtar, S. Zahra.Thermal annealing ambiance effect on phosphorus passivation andreactivation mechanisms in silicon-based Schottky diodeshydrogenated by MW-ECR plasma. *Semicond. Phys. Quantum. Electron. Optoelectron.* 24(4).378-389 (2021).https://doi.org/10.15407/spqeo24.04.378
[23] N. Zirak , M. Shirinbayan , S. Farzaneh , A. Tcharkhtchi,Effect of molecular weight on crystallization behavior of poly (lactic acid) under isotherm and non-isotherm conditions.*Polym. Adv. Technol.* 33 (4), 1307–1316 (2022). https://doi.org/10.1002/pat.5603
[24] Z. Meng , L. Yang, W. Geng, Y. Yao, X. Wang, Y. Liu, Kinetic Study on the Isothermal and Nonisothermal Crystallization of Monoglyceride Organogels. *Sci. World J.* ID 149753, (2014) http://dx.doi.org/10.1155/2014/149753
[25] X. Zhan, L. Wang, J. Wang, Z. Yue , Rui Deng, Y. Wang, X. Xu, Roasting mechanism of lightweight low-aluminum–silicon ceramisite derived from municipal solid waste incineration fly ash and electrolytic manganese residue.*Waste Management*, 153, 264–274 (2022).https://doi.org/10.1016/j.wasman.2022.09.011
[26] M. Martos, M. Martínez, E. Cordoncillo, P. EscribanoTowards more ecological ceramic pigments: Study of the influence of glass composition on the colour stability of a pink chromium-doped ceramic pigment. *J. Eur. Ceram. Soc.* 27(16), 4561-4567 (2007).https://doi.org/10.1016/j.jeurceramsoc.2007.03.030
[27] M. Choudhary, D. Singh, S. K. Jain, S. R. S. Sonawane, D. Singh, G.L. Devnani, K. Srivastava, Kinetics modeling & comparative examine on thermal degradation of alkali treated Crotalaria juncea fiber using model fitting method.*J. Indian Chem. Soc.* 100, 100918 (2023).https://doi.org/10.1016/j.jics.2023.100918
[28] S. Ramukutty, E. Ramachandran, Reaction Rate Models for the Thermal Decomposition of Ibuprofen Crystals *J.cryst. process technol.* 4(2), 71-78 (2014) .DOI:10.4236/jcpt.2014.42010
[29] R. Ahlawat , B. Goswami , N. Rani , G. Rani, Morphological and Photophysical Tempering in Spinel $MgAl_2O_4$ Synthesized by a Novel Citrate Route Via a Suitable Annealing Scheme*J. Electron. Mater.* 52, 1908–1926 (2023). https://doi.org/10.1007/s11664-022-10131-w
[30] S. Dash, R.K. Sahoo, A. Das, S. Bajpai, D. Debasish, S.K.Singh, Synthesis of $MgAl_2O_4$ spinel by thermal plasma and its synergetic structural study.*J. Alloys Compd.* 726, 1186 (2017).https://doi.org/10.1016/j.jallcom.2017.08.085
[31] W. Yuping, L. Xinhong, C. Xiaoyu. Y. Wen, Q. Jia, Evolution of phase composition and microstructure of commercial Al_2O_3 gel in different heat treatment condition. *Ceramics International*. 44(7), 7883-7890 (2018). https://doi.org/10.1016/j.ceramint.2018.01.224
[32] F. Liu, B. A. Goodman, X. Tan, X. Wang, D. Chen, W. Deng, Luminescence and EPR properties of high quality ruby crystals prepared by the optical floating zone method. *Optical Materials*, 91, 183-188 (2019).https://doi.org/10.1016/j.optmat.2019.03.018
[33] A. Mozaffar, H. Masoud, J. Pouria, The role anions on the synthesis of AlOOH nanoparticles using simple solvothermal method.*Bol Soc Esp Cerám Vidr.* 57(2), 66-72 (2017).https://doi.org/10.1016/j.bsecv.2017.06.002
[34] D.S. Kumar, K. Ananthasivan, R.V. Krishnan, S. Amirthapandian,Bulk synthesis of nanocrystalline urania powders by citrate gel-combustion method*J. Nucl. Mater.* 468, 178-193(2016).https://doi.org/10.1016/j.jnucmat.2015.10.054
[35] J. Chandradass, Jae Hong Yoon, Dong-sikBae, Synthesis and characterization of zirconia doped alumina nanopowder by citrate–nitrate process*Mater. Sci. Eng.A.* 473, 360–364 (2008).https://doi.org/10.1016/j.msea.2007.04.115
[36] M.G. Tsegay , H.G. Gebretinsae , Z.Y. Nuru, Structural and optical properties of green synthesized Cr_2O_3 nanoparticles. *Mater. Today: Proc.* 36, 587–590 (2021). https://doi.org/10.1016/j.matpr.2020.05.503
[37] M.Y. Mihaylov, V.R. Zdravkova, E.Z. Ivanova, H.A. Aleksandrov, P.St. Petkov, G.N. Vayssilov , K.I. Hadjiivanov,Infrared spectra of surface nitrates: Revision of the current opinions based on the case study of ceria.*J. Catal.* 394, 245–258 (2021).https://doi.org/10.1016/j.jcat.2020.06.015
[38] N. A. F. Abd Halim, M. K. Bin Yaakob, M. F. Othman, A. Hashim, Syamsyir Akmal Senawi, Wan Aizuddin W Razali,Effect of different fuels on physical, structural and photoluminescence properties of Al_2O_3:Cr^{3+} powder synthesized by solution combustion method. Proceedings of the 2nd Physics and Materials Science International Symposium (PhyMaS 2.0) AIP Conf. Proc. 2368, 030008-1–030008-10; (2021). https://doi.org/10.1063/5.0058592